Imdad Uddin Chowdhury, Pallab Sinha Mahapatra [ID], and Ashis Kumar Sen [ID]

COLLECTIONS

F   This paper was selected as Featured

View Online   Export Citation   CrossMark

ARTICLES YOU MAY BE INTERESTED IN

Influence of textural statistics on drag reduction by scalable, randomly rough superhydrophobic surfaces in turbulent flow
Physics of Fluids **31**, 042107 (2019); https://doi.org/10.1063/1.5090514

Effects of shear intensity and aspect ratio on three-dimensional wake characteristics of flow past surface mounted circular cylinder
Physics of Fluids **31**, 043602 (2019); https://doi.org/10.1063/1.5081795

Formation of water in oil in water particles by drop impact on an oil layer
Physics of Fluids **31**, 037107 (2019); https://doi.org/10.1063/1.5089001

Self-driven droplet transport: Effect of wettability gradient and confinement ⒡

View Online   Export Citation   CrossMark

Imdad Uddin Chowdhury, Pallab Sinha Mahapatra,[a] ⒾⒹ **and Ashis Kumar Sen** ⒾⒹ

AFFILIATIONS

Department of Mechanical Engineering, IIT Madras, Chennai 600036, India

[a]Author to whom correspondence should be addressed: pallab@iitm.ac.in

ABSTRACT

Surface tension driven droplet transport in an open surface is increasingly becoming popular for various microfluidic applications. In this work, efficient transport of a glycerin droplet on an open wettability gradient surface with controlled wettability and confinement is numerically investigated. Nondimensional track width w^* (ratio of the width of the wettability gradient track w and the initial droplet diameter d_0) of a wettability gradient track laid on a superhydrophobic background represents wettability confinement. A lower value of w^* represents higher wettability confinement. Droplet behavior changes for different wettability confinements and gradients of the track. It is found that droplet velocity is a function of the wettability confinement and the gradient; droplet transport velocity is maximum for $w^* = 0.8$. Higher confinement ($w^* < 0.8$) leads to a significant reduction in droplet velocity. Droplet transport characteristics on hydrophilic–superhydrophilic, hydrophobic–superhydrophilic, and superhydrophobic–superhydrophilic tracks are studied. It is found that for a fixed length of the track, droplet velocity is maximum for the superhydrophobic–superhydrophilic track. A droplet transport regime is demonstrated for a wettability gradient track with different confinements, and it is found that the droplet is transported for wettability confinement $w^* > 0.6$ irrespective of the wettability gradient of the track. These findings provide valuable insight into efficient droplet manipulation in microfluidic devices.

Published under license by AIP Publishing. https://doi.org/10.1063/1.5088562

I. INTRODUCTION

Droplet motion on a wettability controlled open surface has broad prospective in different areas starting from textiles to microfluidic devices and heat exchangers.[1,2] Droplet transport on a microfluidic device has the challenges because of the dominance of surface force over inertia force. Transport of a droplet without an external power source in a microfluidic device is possible by using a surface tension gradient. Laplace pressure driven droplet transport in an open surface by using wedge-shaped superhydrophilic tracks laid on a superhydrophobic background was demonstrated by Ghosh *et al.*[3] They developed an efficient wedge-shaped track for high rate pumpless liquid transport for the application of a lab-on-a-chip (LOC) system. The various other ways of transporting a droplet on surfaces are by creating a thermal gradient on the surface,[4–7] electrowetting,[8–11] magnetic field,[12] light-induced droplet transport,[13] shape gradient droplet transport,[14–16] and by using chemical or physical textured gradient,[17–19] which is known as wettability gradient. All the techniques other than wettability gradient and shape gradient are intrusive, i.e., the techniques may alter the properties of

the liquid droplet.[20] When a droplet is placed on a wettability gradient solid surface, a droplet tends to move from the low wettable region to high wettable region due to the net driving force along the direction of increasing surface wettability. This net driving force is due to the curvature difference between the front and rear half of the droplet.

Greenspan[21] and Brochard[22] performed a detailed analytical study on droplet manipulation by a wettability gradient on a surface, for the first time. Subramanian *et al.*[23] analyzed the forces involved during the motion of a droplet on a solid surface due to surface wettability gradient. They demonstrated the hydrodynamic resistance offered by the droplet by approximating the droplet shape as the collection of wedges which is known as "wedge approximation." They also highlighted the hydrodynamic resistance by using the lubrication theory approximation. The first experimental observation of droplet transport on a wettability gradient surface was demonstrated by Chaudhury *et al.*[24] They showed that it is possible to run a water droplet uphill up to an inclination angle of ~10°. Moumen *et al.*[25] performed detailed experiments on droplet transport on a horizontal solid surface using a wettability gradient. They observed that the

velocity of the droplet is a function of the position of the droplet. Velocity increases up to a certain distance along the direction of the droplet motion, and it decreases further. They assumed the quasisteady approximation to calculate the droplet velocity, theoretically. Chaudhury et al.[26] showed various ways of droplet transport on a solid surface. They also showed multiple methods of preparing wettability gradient surfaces. Bliznyuk et al.[27] designed a smart striped patterned gradient surface to control the droplet spreading in a particular direction. They used an alternating hydrophilic and hydrophobic strip. Wherein they observed that spreading of a droplet on a smart patterned gradient surface is faster compared to a normal wettability gradient surface. However, preparation of such a thin alternating patterned strip is quite challenging. Ito et al.[28] have experimented with droplet motion on a wettability gradient surface and found out that droplet velocity increases with the increase in wettability gradient of the surface. Liu et al.[29] have prepared a wettability gradient surface from superhydrophobic static contact angle (166°) to superhydrophilic static contact angle (15.5°). They have experimented with both the nanopillar-Si surface and plane-Si surface and observed that for the nanopillar-Si gradient surface, the driving force is higher and resistive force is lower compared to the plane-Si gradient surface.

Xu and Qian[18] numerically analyzed the motion of a nanometer-sized droplet on a heated solid substrate with wettability gradients. They accurately modeled the fast variation of temperature from solid to fluid. Their numerical result showed that droplet velocity is proportional to the wettability gradient as predicted by Brochard.[22] The proportionality constant is found to be linearly dependent on the ratio of the slip length to the initial droplet diameter. Liu and Xu[30] performed the theoretical and molecular dynamic simulation of transport of the water droplet on a wettability gradient surface. Raman[31] used the phase field based Lattice Boltzmann Method (LBM) to simulate the dynamics of two droplet coalescence on the wettability gradient surface. They observed that when drops impinge on a wettability gradient surface, impact shape of the droplets deviates from the spherical shape that leads to different droplet morphologies near the connecting region of the droplet and higher spreading factor. Huang et al.[32] performed the 2D numerical simulation of droplet transport on a stepwise wettability gradient surface by considering contact angle hysteresis (CAH) on the surface. They used the Lattice Boltzmann Method (LBM) and found that the velocity of the droplet has a strong dependency on viscosity ratio, wetting gradient magnitude, and CAH. Ahmadlouydarab and Feng[33] numerically investigated the motion and coalescence of a droplet by using a wettability gradient and external flow. They also analyzed the transport of a single droplet on a wettability gradient surface and validated the results with theoretical prediction (wedge flow model) and experimental results of Moumen et al.[25] Huang et al.[34] investigated the manipulation of a droplet by spatiotemporal variation of wettability of the surface by using the Lattice Boltzmann Method (LBM). They observed that droplet transport is faster for alternating nonwetting and wetting units with proper nonwetting confined stripes. Various droplet responses are observed for different surface wettability controls. They optimized the size of the confined strips and substrate wettability frequency by taking substrate wettability as a single step gradient.

Although various researchers have performed experimental and numerical studies on droplet transport on a uniform wettability gradient surface, the behavior of a droplet on a confined wettability gradient surface is unexplored. In the lab-on-a-chip (LOC) system, due to the space constraint, it is essential to use the minimal track width for droplet transport on an open surface. An attempt is being made in the present work to obtain the wettability confined track width for efficient droplet transport in an open microfluidics platform. The behavior of a droplet under various wettability gradients and confinements of the surface is analyzed. This fundamental study provides essential insight into passive droplet manipulation on open surface microfluidic devices.

II. NUMERICAL MODELING

Among the different conventional numerical methods that are available to solve the two-phase flow situation, the Finite Element Method (FEM) is a more robust technique. We have used FEM based computational fluid dynamics (CFD) tool COMSOL Multiphysics for modeling the problem. To track the interface, the Level Set Method[35] is used. In this method, the interface is continuous, and the calculation of the curvature and surface tension force is much more accurate compared to the Volume of Fluid (VOF) method.[35] The interface is modeled by using a level set function ϕ whose value varies from 0 to 1. The value of ϕ is 0 for lighter fluid and 1 for a heavy fluid. In the present work, lighter fluid is air, and heavier fluid is glycerin. The nature of the interface is "diffuse" and we approximated the value of ϕ at the interface is 0.5. The level set function ϕ is advected with the flow and hence the interface. The following equation is solved to track the interface:[36–38]

$$\frac{\partial(\phi)}{\partial t} + u \cdot \nabla \phi = \gamma \nabla \cdot \left(\epsilon \nabla \phi + \phi(1 - \phi) \frac{\nabla \phi}{|\nabla \phi|} \right). \quad (1)$$

At the sharp interface, a discontinuity appears when the fluid parameter changes at the interface. To avoid this difficulty, the interface thickness ϵ is defined, so the fluid parameter changes smoothly. The value of $\epsilon(m)$ is taken as half of the grid spacing h_1.[36] The level set function ϕ varies linearly across the interface. The parameter γ determines the amount of reinitialization or stabilization of the level set function. The value of γ needs to be tuned for a specific problem. If γ is too small, the thickness of the interface might not remain constant, and oscillations in ϕ may appear because of numerical instabilities. On the other hand, if γ is too large, the interface moves incorrectly. A suitable value for γ is the maximum magnitude of the velocity field u. To identify the sensitivity of γ, several simulations were performed with the γ values in the ranges of 1 m/s to 1×10^{-4} m/s. We have found out that for γ in the range of $0.1–10^{-4}$ m/s (which is the range of expected contact line speed), there is no effect of γ on the dynamics of the droplet transport. Therefore, in the present simulations, we have chosen γ to be 0.1 m/s.

Two fluids are considered to be immiscible. Flow is assumed to be laminar, incompressible, Newtonian, and isothermal. The two-phase flow can be described by following a set of governing equations in the Cartesian coordinate system

$$\nabla \cdot \mathbf{u} = 0, \quad (2)$$

$$\rho_a \frac{\partial \mathbf{u}}{\partial t} + \rho_a (\mathbf{u} \cdot \nabla)\mathbf{u} = \nabla \cdot \left[p\mathbf{I} + \mu_a (\nabla \mathbf{u} + \nabla \mathbf{u}^{\mathbf{T}}) \right] + \rho \mathbf{g} + \mathbf{F_{st}}, \quad (3)$$

where $\mathbf{F}_{st}$ (N/m^2) is the interfacial force, $\mathbf{u}$ (m/s) is the velocity of the fluid, t (s) is the time, p (Pa) is the fluid pressure, $\mathbf{I}$ is the position vector, ρ_a (kg/m^3) is the average density of the two fluid, and μ_a (Pa s) is the average viscosity of the two fluid. Both ρ_a and μ_a are considered to be smooth at the interface and are calculated from level set function ϕ as follows:

$$\rho_a = \rho_1 + (\rho_2 - \rho_1)\phi, \tag{4}$$

$$\mu_a = \mu_1 + (\mu_2 - \mu_1)\phi. \tag{5}$$

From Eqs. (4) and (5), if the value of ϕ is considered as 0, then the average density $\rho_a = \rho_1$, where ρ_1 is the density of the lighter fluid, air. Hence, $\phi = 0$ represents the air phase. Similarly, $\phi = 1$ represents the droplet phase which is the heavier fluid. The surface tension force $\mathbf{F}_{st}$ used in Eq. (3) can be expressed as

$$\mathbf{F}_{st} = \sigma\kappa\delta\hat{\mathbf{n}}, \tag{6}$$

where σ (N/m) is the surface tension force, κ (1/m) is the curvature of the droplet, δ (m) is Dirac's delta function which represents the interface of the droplet. The curvature of the droplet is κ, and the interface normal $\hat{\mathbf{n}}$ is defined as

$$\hat{\mathbf{n}} = \frac{\nabla\phi}{|\nabla\phi|}, \tag{7}$$

$$\kappa = -\nabla\cdot\hat{\mathbf{n}}. \tag{8}$$

All the boundaries are considered as "outlet" with zero pressure except the wetted bottom wall. In the wetted wall, linear variation of the static contact angle is prescribed. It is also assumed that the surface has negligible hysteresis. In the wetted wall, the Navier slip boundary condition is adopted and the contact angle between the wetted wall and the interface of the two-phase fluid is assigned. The Navier slip boundary condition of the interface along the wetted wall adds a frictional force of the form,[38]

$$\mathbf{F}_{fr} = \frac{\mu_\phi}{\beta}\mathbf{u}. \tag{9}$$

In the present work, the slip length is taken as half of the grid size ($0.5h_1 \sim \mu$m).[36,38] To numerically resolve the droplet motion by avoiding the multiscale modeling approach, a comparatively large slip length is considered. We have identified that for $\beta \leq 0.5h_1$, the numerical solutions are insensitive to the choice of β. For β much less than the grid size h_1, the slip length is not resolved numerically and hence the slip velocity $\mathbf{u} \to 0$ at the wetted wall as well as the F_{fr}. When $F_{fr} \to 0$, the boundary condition in the wall is similar to the no-slip condition. Another boundary condition at the wetted wall is no penetration of fluid at the wall, which is defined as

$$\mathbf{u}\cdot\hat{\mathbf{n}}_{\mathbf{wall}} = 0. \tag{10}$$

The unit normal vector to the wall is $\hat{\mathbf{n}}_{\mathbf{wall}}$. The above wetted wall boundary conditions do not set the tangential velocity component to be 0. Instead, the tangential velocity component is 0 at an extrapolated distance β outside of the wetted wall. In the level set method, given the contact angle at the wall as θ, a weak boundary term adds in the wetted wall boundary condition[38]

$$\int_{\delta\Omega}\chi(\mathbf{u})[\sigma(\hat{\mathbf{n}}_{\mathbf{wall}} - \hat{\mathbf{n}}\cos\theta)\delta]dS. \tag{11}$$

This boundary term obtained from the partial integration of the surface tension force $\mathbf{F}_{st}$ of the momentum equation is shown in Eq. (3). The narrow weighted function around the contact line at the wetted wall is represented by $\chi(\mathbf{u})$. The total force on the wetted wall is[38]

$$\mathbf{F}_{\mathbf{wall}} = \sigma(\hat{\mathbf{n}}_{\mathbf{wall}} - \hat{\mathbf{n}}\cos\theta)\delta - \frac{\mu_\phi}{\beta}\mathbf{u}. \tag{12}$$

Modeling of the laminar two-phase flow using level set method was performed on the computational fluid dynamics module of a COMSOL Multiphysics solver. The grid-independent test was performed, and the nondimensional grid size of $\frac{h_1}{d_0} = 0.11$ is found to be the independent grid. Here, d_0 is the initial droplet diameter. Physics controlled adaptive time stepping is used for all the simulations.

A. Problem setup

A glycerin droplet of diameter d_0 is placed on a confined wettability gradient surface. As shown in the Fig. 1, the computational domain dimension is $L \times B \times H$. L represents the length of the surface, the width of the surface is B, and H represents the height of the computational domain. The density of the glycerin droplet is $\rho_2 = 1220$ kg/m^3, the viscosity is $\mu_2 = 0.116$ Pa s, and the surface tension of the droplet is $\sigma = 0.063$ N/m. The surrounding medium is air. The density of air is $\rho_1 = 1.12$ kg/m^3, and the viscosity is $\mu_1 = 1.8 \times 10^{-5}$ Pa s. The surrounding medium and the droplet are at room temperature, and the changes in the properties due to temperature variation are negligible. No initial impact velocity is provided to the droplet. Droplet diameter is taken to be much smaller than the capillary length scale ($B_0 \ll 1$); thus, the gravity effect is negligible. It is observed that for droplet diameter less than 1 mm, there is no effect of gravity on the droplet transport. Hence, all the simulations were carried out with droplets of diameter less than 1 mm. The nondimensional parameters used in the present work are, nondimensional center position of the droplet $x^* = x/L$, nondimensional center of mass of the droplet along the direction of droplet transport $x_c^* = x_c/L$, nondimensional front position $x_f^* = x_f/L$, nondimensional height $h^* = h/L$, nondimensional wetted area
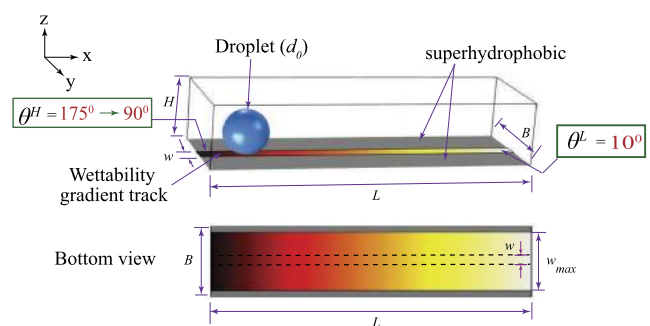

FIG. 1. A glycerin droplet of diameter d_0 is placed on a confined wettability gradient surface of length $L = 7d_0$ and width $B = 2.5d_0$. The height of the computational domain is taken as $H = 1.5d_0$. The downstream contact angle of the confined wettability gradient track θ^L fixed as 10°. The upstream contact angle of the confined track θ^H varies from 175° to 90° to obtain different wettability gradients. The droplet is placed at a distance d_0 from left to eliminate the effect of the left boundary on the droplet. The wettability confined track width is w. The maximum wettability confined track width is $w_{max} = 2d_0$. Both sides of the wettability confined gradient track are superhydrophobic (contact angle = 175°).

$A^* = A(t)/A_0$, nondimensional time $t^* = t\sigma/L\mu_1$, nondimensional track width $w^* = w/d_0$, and capillary number of the droplet $Ca = \mu_1 U/\sigma$. The droplet center position is represented by x. The center of mass of the droplet along the direction of droplet transport is represented by x_c^*. The front position of the droplet is x_f, the height of the droplet is h, the transient wetted area of the droplet represented by $A(t)$. $A_0 = \pi d_0^2/4$ represents the initial droplet footprint area. The velocity of the droplet is U. Uniform wettability gradient is considered, and the variation of contact angle on the wettability gradient track is

$$\theta = \theta^H - \frac{(\theta^H - \theta^L)}{L}x. \tag{13}$$

Wettability gradient is defined as $\lambda = \frac{(\theta^H - \theta^L)d_0}{L}$. It is assumed that initially, the droplet is having a point contact with the wettability gradient track and hence the droplet initial contact angle can be considered as $180°$. For a hydrophilic–superhydrophilic wettability gradient track, a sharp spreading of the droplet occurs within a few fractions of milliseconds because of the difference in the initial surface energies between the droplet and the surface. Nondimensional track width w^* denotes the wettability confinement. For track width w greater than d_0 (i.e., $w^* > 2$), it is observed that there is no significant effect of wettability confinement on the droplet transport. Wettability confinement increases by decreasing the value of w^*.

B. Validation

To validate our simulation approach using the COMSOL Multiphysics solver, the steady state simulation is performed in the HyDro simulation solver developed by Matsui *et al.*[39] HyDro has an efficient algorithm to simulate the equilibrium shape of a microscale droplet placed on a surface with hydrophilic-hydrophobic patterning. This solver uses hybrid energy minimization techniques to get the equilibrium shape of a microdroplet. To validate our problem, the droplet is placed at the junction of the wettability gradient step.

As our focus is on the confined wettability gradient surface, the step wettability gradient surface is considered to have confined wettability for different w^*. The droplet moves from a lower wettable region to a higher wettable region and attains a final steady-state shape of the droplet. Simulations are performed for two different wettability confinements $w^* = 0.8$ and $w^* = 0.4$. The lower value of w^* represents higher wettability confinement. It is observed that steady state droplet spreading is more and height is less in a more wettability confinement track. Validation of height, spreading, and 3D shape of the droplet obtained from the COMSOL simulation is compared with HyDro, which is shown in Fig. 2. A very good agreement (within 5%) between the COMSOL simulation and HyDro solver is found.

To validate the transient behavior of our solver, a flat immersion oil droplet is placed at the junction of a wettability step gradient surface [see Fig. 3(a)]. Density of the droplet is $\rho = 923$ kg/m^3, dynamic viscosity is $\mu = 0.098$ Pa s, and surface tension is $\sigma = 0.037$ N/m. The droplet radius is taken as $R = 1.5$ mm. The surrounding medium of the droplet is air. In the present simulations, the capillary number $Ca = \mu V_{drop}/\sigma$ is calculated for the average velocity of the droplet V_{drop}. Theoretical prediction of the capillary number for a flat droplet on a stepwise wettability gradient surface is calculated as[32]

$$Ca = \frac{1}{6l}\sqrt{\frac{\theta_1^2 + \theta_2^2}{2}}\left(\frac{\theta_1^2 - \theta_2^2}{2}\right), \tag{14}$$

where $l = \ln(k_l/\epsilon_1)$ is the constant prefactor. Nondimensional slip length, $\epsilon_1 = l_s/L = 1.33 \times 10^{-2}$. The slip length is represented by l_s. In a real system, the slip length is usually of molecular scale ($\sim 10^{-9}$), and it is beyond our capability to numerically resolve such small slip length.[32] In the present validation, the slip length is taken as $20\,\mu m$,[32] which is 2–3 order higher than the real slip length. k_l is a constant whose value is taken as 0.152.[32] It is observed from Fig. 3(b) that the capillary number of the droplet (Ca) increases with the increase
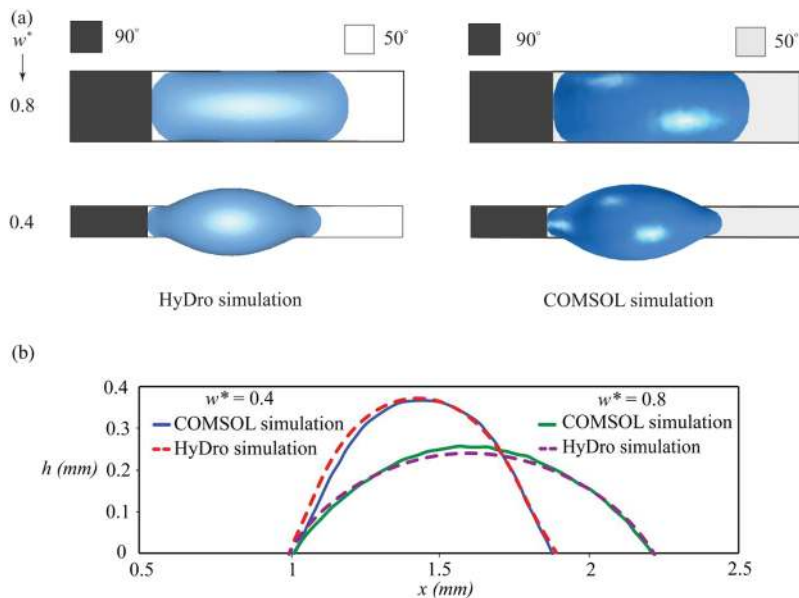

FIG. 2. A glycerin droplet of diameter $d_0 = 0.5$ mm is placed on a confined wettability step gradient surface. Initial droplet position is at the junction of the wettability gradient step of $90°$ and $50°$. (a) 3D droplet shape of HyDro solver and COMSOL simulations in the final steady state. (b) Comparison of h vs x from HyDro solver and COMSOL simulations for two different wettability confinements w^*. Outside of the step wettability gradient track is taken as superhydrophobic (contact angle = $175°$).
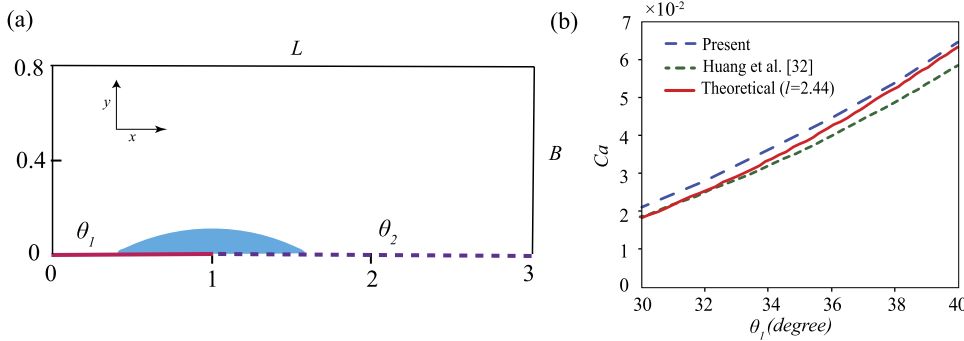
FIG. 3. A flat immersion oil droplet is placed on a wettability step gradient surface having a computational 2D domain dimension of 3 mm × 0.8 mm as shown in (a). R is the initial radius of the droplet, and its initial position is $(-\sqrt{3}R/2, L/3)$. For $x < L/3$, $\theta = \theta_1$, and for $x \geq L/3$, $\theta = \theta_2$. Downstream contact angle, θ_2, is maintained at 23° and upstream contact angle, θ_1, is varying from 30° to 40°. (b) The variation of capillary number of the droplet with different wettability step gradients.

in wettability gradient due to the increase in the driving force. The present numerical work and the numerical work by Huang et al.[32] have almost the same difference (within 5%) with the theoretical results obtained from Eq. (14). The difference between the present numerical work and the numerical work by Huang et al.[32] is because of the two different numerical modeling approaches. We used the level set method for interface tracking, whereas Huang et al.[32] have used the phase field method to track the interface. In the level set method, we solve an algebraic equation of level set function ϕ to track the interface. On the other hand, in the phase field method, the interface is determined by minimizing the free energy.

III. RESULTS AND DISCUSSION

The response of a droplet on a wettability gradient surface is fascinating. The droplet tends to move from a low wettable region to a high wettable region due to the curvature difference between the rear and front of the droplet. The droplet velocity is proportional to this curvature difference. In the present work, initial droplet diameter d_0 is taken such that the gravity effect can be neglected. The hysteresis on the surface is assumed to be negligible. Hence, there are two significant forces which govern the movement of the droplet. One is the driving force, F_d, due to the contact angle difference between the rear and front of the droplet. The other force is the hydrodynamic resistance force, F_r, exerted by the solid surface on the droplet which tends to resist the droplet movement. The resultant net force $(F_d - F_r)$ is responsible for the droplet transport. When a liquid droplet is placed on a confined wettability track, it forms an elongated bulged shape due to the wettability gradient as shown in Fig. 4. In the pinned liquid boundary, one additional force is added in the direction of droplet transport due to the wettability confinement. It is observed that the force due to the confinement effect is smaller in magnitude as compared to the major driving force which is due to the contact angle difference. The driving force F_d and the hydrodynamic resistance force F_r are derived from Ref. 23, as shown in the Appendix. The approximated F_d and F_r are expressed as

$$F_d \approx A(t)\sigma \frac{d\cos\theta}{dx}, \qquad (15)$$

$$F_r \approx \frac{6\pi R(t)\mu_2 U}{\theta_{avg}(t)}\ln(2\epsilon), \qquad (16)$$

where σ denotes the surface tension of the droplet. Dynamic viscosity of the droplet is μ_2, and the velocity of the droplet is U.

The contact angle of the droplet with the wetted wall is $\theta_{avg}(t) \approx ((\theta_e)_f(t) + (\theta_e)_b)(t)/2$ which is changing during the transport of the droplet. The front static contact angle of the droplet is $(\theta_e)_f(t)$, and the rear static contact angle is $(\theta_e)_b(t)$. The dimensionless parameter $\epsilon = l_{s1}/R(t)$ represents the ratio of the slip length l_{s1} to the footprint radius or wetted radius $R(t)$ of the droplet. The transient wetted area of the droplet $A(t)$ is calculated by surface integration of the droplet footprint, i.e., $A(t) = \iint_S dx\,dy$ (for $\phi \geq 0.5$). As the footprint of the droplet is not circular, therefore, we have approximated $R(t) \sim \sqrt{A(t)}$.

The net driving force $(F_d - F_r)$ drives the droplet. A detailed description of the change in capillary number Ca during the droplet transport is presented in the Appendix. Using scaling analysis, a scaled capillary number is derived from F_d and F_r and the effect of the different parameters on the Ca is described.

A. Effect of wettability confined droplet transport on a hydrophilic–superhydrophilic wettability gradient track

A glycerin droplet of diameter d_0 is placed on a uniform wettability gradient track of length $L = 7d_0$ with different wettability
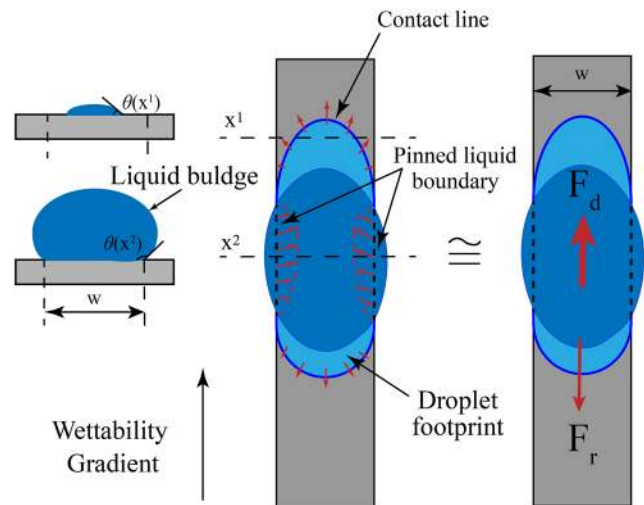

FIG. 4. A droplet placed on a wettability confined gradient surface having confinement width w. Due to the confinement, the droplet is bulge shaped and elongated in the moving direction. Force balance is showed by red arrow lines.

confinements w^*. A wettability gradient of the track is defined as $\lambda = \frac{(\theta^H - \theta^L)d_0}{L}$. The upstream contact angle is denoted by $\theta^H = 90°$, and the downstream contact angle is denoted by $\theta^L = 10°$. Thus, the wettability gradient for the present case is 11.5. As shown in Fig. 5(a), at $t^* = 22$, the droplet does not reach the end of the track for all w^*. It is also observed that spreading of the droplet in the direction of the droplet transport is also different for different wettability confinements (w^*). Spreading of the droplet in the direction of droplet transport is highest for $w^* = 0.8$. Higher spreading in the direction of the droplet transport increases the value of $(\cos(\theta_e)_f - \cos(\theta_e)_b)$ and hence the driving force F_d as shown in Eq. (15). As the driving force F_d is the highest for $w^* = 0.8$, the droplet velocity is maximum for $w^* = 0.8$. Figure 5(b) shows that the droplet is having highest x_f^* for $w^* = 0.8$, which means that the droplet reaches the end of the track faster for $w^* = 0.8$ compared to all other w^*. It is observed in Fig. 5(c) that for $t^* = 22$, the nondimensional center of mass of the droplet along the direction of the droplet transport x_c^* is nearly identical for $w^* = 2$ to $w^* = 0.8$, and it decreases for $w^* \leq 0.8$. In the present study, we considered the racing of droplets on different wettability confinement tracks and the track on which the droplet touches the end first is considered as the most efficient track. Up to wettability confinement $w^* = 0.8$, droplet velocity increases. Further increase in the wettability confinement by decreasing the value of w^* leads to a rapid decrease in droplet velocity; this is because of the restrictions in spreading of the droplet in the lateral direction for higher wettability confinement.

Although spreading of the droplet in the direction of the droplet transport is highest for $w^* = 0.8$, the overall wetted area is maximum for $w^* = 2$, as shown in Fig. 6(a). For $w^* = 2$, the droplet can spread freely in both the directions and hence nondimensional wetted area A^* is maximum. An increase in wettability confinement

leads to a decrease in A^* because of the restriction on spreading of the droplet in the lateral direction. The initial sharp increase in nondimensional wetted area A^* with t^* is because of the initial surface energy difference between the droplet and the wettability gradient track as discussed in Subsection II A. Droplet spreads fast and attains the surface contact angle within 1 ms of touching the surface for all different wettability confinements w^* studied here. The initial spreading speed (velocity) of the droplet for $w^* = 2$ is 22 mm/s, and it is nearly the same up to $w^* = 0.8$. Due to the confinement, the droplet speed reduces significantly for $w^* \leq 0.8$. The initial droplet velocity on the $w^* = 0.4$ confined track is 13 mm/s. Figure 6(a) shows that the increase in A^* with t^* after initial spreading of the droplet is approximately linear ($R^2 \sim 0.98$) for all different w^*. The inset of Fig. 6(a) shows the variation of slope of the curve m with w^*. It is observed that the slope m is the highest for $w^* = 2$ ($m = 0.11$). From $w^* = 2$ to $w^* = 0.8$, m decreases linearly from 0.11 to 0.075. However, m decreases linearly from 0.075 to 0.016 for $w^* = 0.8$ to $w^* = 0.4$. The rate of decrease in the slope m from $w^* = 2$ to $w^* = 0.8$ is less than the rate of decrease in the slope m for $w^* \leq 0.8$ as shown in the inset of Fig. 6(a). Figure 6(b) shows that the nondimensional height of the droplet h^* decreases with increasing w^*. This is due to the restriction of spreading of the droplet in the lateral direction during transport. The inset of Fig. 6(b) shows the variation of m with w^*. It is observed that from $w^* = 2$ to $w^* = 0.8$, m is approximately constant ($m = -0.465$), whereas the slope m increases linearly from -0.465 to -0.158 for $w^* = 0.8$ to $w^* = 0.4$. The increase in slope m for $w^* \leq 0.8$ is linear.

For a wettability gradient of 11.5 (hydrophilic–superhydrophilic surface), the maximum wettability confinement of $w^* = 0.3$ can be achieved. Further confinement leads to the insufficient driving force due to less spreading, and hence the droplet does not move. Figure 6(c) shows that nondimensional time t^* taken by the droplet front to reach the end of the track is minimum for $w^* = 0.8$.
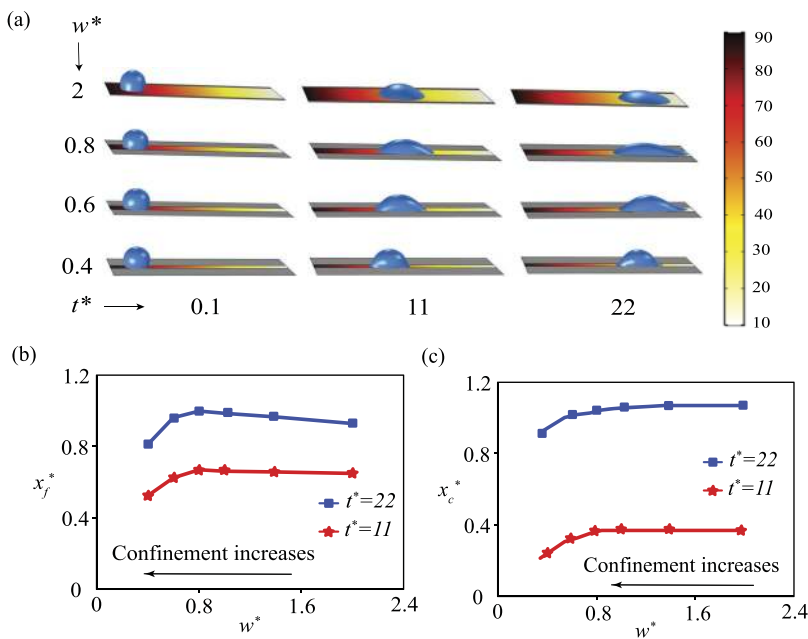

FIG. 5. A droplet of initial diameter $d_0 = 0.5$ mm is placed on a wettability confined gradient surface having nondimensional wettability confinement w^*. (a) Droplet position and shape with different t^*. (b) Variation of nondimensional droplet front position x_f^* for different wettability confinements w^* is plotted for two different t^*. (c) Variation of nondimensional center of mass of the droplet along the direction of the droplet transport x_c^* for different w^* is plotted for two different t^*.
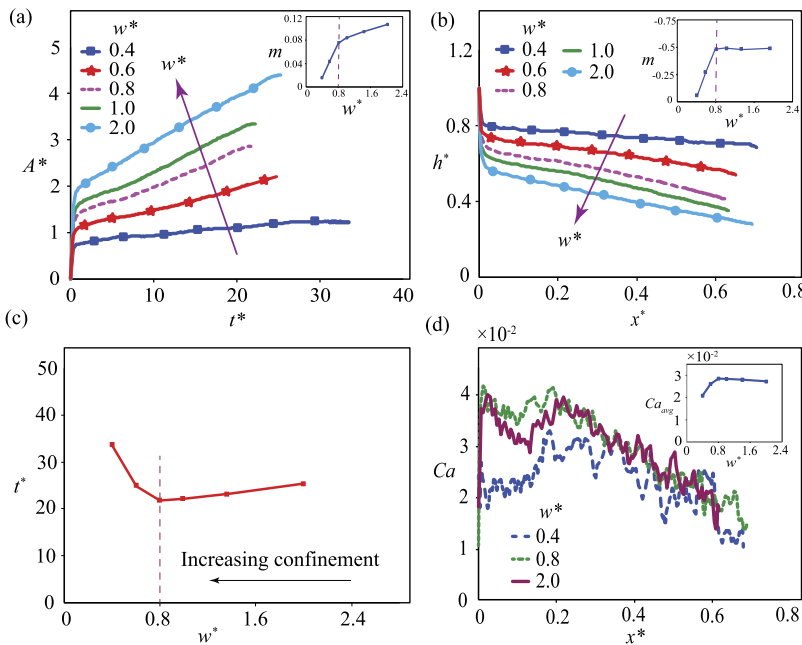
FIG. 6. (a) Variation of the nondimensional wetted area of the droplet with nondimensional time t^* plotted for different wettability confinements w^*. Slope of the linear part of each curve is represented by m. (b) Variation of the nondimensional height of the droplet h^* plotted with the nondimensional position of the droplet x^* for different w^*. (c) Variation of nondimensional time t^* taken by the droplet front to reach the end of the track is plotted with different w^*. (d) Variation of the capillary number of the droplet Ca with the nondimensional position of the droplet x^* plotted for different w^*.

Hence, $w^* = 0.8$ is the most efficient wettability confinement in a hydrophilic-superhydrophilic wettability gradient track that offers the best performance in terms of droplet transport. As observed in Fig. 6(d), the droplet capillary number Ca initially increases sharply within 1 ms which is due to the sharp initial spreading of the droplet. After that, Ca increases up to $x^* = 0.18$ to a maximum value of 0.041. On the other hand, Ca decreases for $x^* \geqslant 0.18$. This change in the Ca is because of the velocity of the droplet, and the velocity of the droplet is a function of F_d and F_r. The driving force F_d is dependent on the transient wetted area of the droplet $A(t)$ and $d \cos \theta/dx$, as shown in Eq. (15). The effect of $A(t)$ and $d \cos \theta/dx$ on F_d is discussed in the Appendix. As shown in Eq. (16), the resistive force F_r is dependent on the velocity of the droplet U and the wetted radius $R(t) \sim \sqrt{A(t)}$. The effect of U and $R(t)$ on F_r is discussed in the Appendix.

The net driving force $(F_d - F_r)$ is responsible for driving the droplet. Up to $x^* = 0.18$, F_d and F_r are increasing, and also, the net driving force $(F_d - F_r)$ is increasing. Therefore, the capillary number of the droplet Ca increases downstream and reaches a maximum value of 0.041 at $x^* = 0.18$. $F_d - F_r$ start decreasing for $x^* \geqslant 0.18$, and thus, Ca decreases [refer to Fig. 12(a) in the Appendix]. Scaling of Ca is performed using the expression of F_d and F_r as shown in the Appendix. The change in the numerical value of Ca during the droplet transport is found to have a good agreement with Ca obtained from the scaling analysis [see Fig. 11(a) in the Appendix]. The average capillary number of the droplet Ca_{avg} represents the average velocity of the droplet during the transport. The inset of Fig. 6(d) clearly shows that Ca_{avg} is maximum for wettability confinement $w^* = 0.8$. Therefore, it is advisable to use wettability confinement up to $w^* = 0.8$ for all practical purposes, further confinement $(w^* < 0.8)$ leads to a sharp reduction in Ca_{avg}.

B. Effect of wettability gradient λ on confined wettability gradient track of $w^* = 0.8$

From the above study, we found out that wettability confinement $w^* = 0.8$ is the most efficient confinement for wettability gradient $\lambda = 11.5$. Therefore, the effect of different wettability gradients λ for $w^* = 0.8$ is studied. The downstream contact angle of the confined track is fixed at $\theta^L = 10°$, and the upstream contact angle θ^H varies from $175°$ to $90°$ as shown in the problem description in Fig. 1. As θ^L is fixed at $10°$, the different values of θ^H represent different wettability gradients λ for a fixed length of the track. λ for the present case varies from 11.5 to 23.5. As shown in Fig. 7(a), the variation of nondimensional wetted area of the droplet (A^*) with nondimensional time (t^*) is linear $(R^2 \sim 0.99)$. The inset of Fig. 7(a) shows the variation of slope of the curve m with λ. It is observed that m is the highest $(m = 0.2)$ for $\lambda = 23.5$. The slope m increases from 0.075 to 0.2 linearly with the increase in λ from 11.5 to 23.5. Due to the minimal initial surface energy difference between the droplet and the surface, there is no initial sharp spreading of the droplet [see Fig. 7(a) for $\lambda = 23.5$].

Figure 7(b) shows that droplet capillary number Ca increases with the nondimensional position of the droplet x^* for over an initial distance due to the dominance of the driving force F_d over the hydrodynamic resistance force F_r. After that, the droplet capillary number decreases. For $\lambda = 11.5$, the dominance of driving force over the hydrodynamic resistance force was obtained up to $x^* = 0.18$, whereas for $\lambda = 11.5$, it is up to $x^* = 0.5$ as shown in Fig. 7(b). For higher λ, the peak of the net driving force $(F_d - F_r)$ shifts toward downstream and hence the shift of the Ca peak as shown in Figs. 12(a) and 12(b) of the Appendix. This shift of Ca peak is true for any wettability confinement w^*. Scale analysis of F_d and F_r is performed as shown in the Appendix and the change in numerical capillary number Ca during the droplet transport for two different
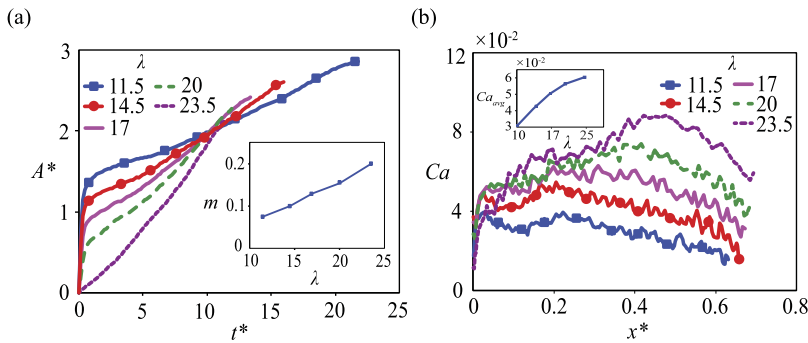
FIG. 7. (a) Nondimensional wetted area of the droplet A^* with nondimensional time t^* is plotted for different wettability gradients of the track λ. Slope of the linear part of each curve is represented by m. (b) The variation of capillary number of the droplet Ca with nondimensional position of the droplet x^* is plotted for different λ.

wettability gradients λ is found to have a good agreement with the scaled capillary number [refer to Figs. 11(a) and 11(b) of the Appendix]. The average capillary number of the droplet Ca_{avg} increases with the increase in λ as shown in the inset of Fig. 7(b). The average capillary number is maximum for $\lambda = 23.5$. Hence, for the $w^* = 0.8$ wettability confined gradient track, $\lambda = 23.5$ (superhydrophobic–superhydrophilic) offers higher droplet velocity. The average capillary number Ca_{avg} of the droplet is nearly double for the $\lambda = 23.5$ (superhydrophobic–superhydrophilic) track compared to the $\lambda = 11.5$ (hydrophilic–superhydrophilic) track [see Fig. 7(b)].

C. Effect of w^* on droplet transport for superhydrophobic–superhydrophilic wettability gradient track

From the above, we observed that wettability confinement $w^* = 0.8$ and wettability gradient $\lambda = 23.5$ offer the best performance for droplet transport. In a surface of a wettability gradient of $\lambda = 11.5$ (hydrophilic–superhydrophilic), maximum wettability confinement can be achieved with as small as $w^* = 0.3$. However, it is possible to achieve wettability confinement as small as $w^* = 0.1$ by considering the wettability gradient of the surface to be $\lambda = 23.5$ (superhydrophobic–superhydrophilic), this is because that the droplet has a higher driving force F_d in the case of $\lambda = 23.5$ compared to $\lambda = 11.5$. Hence, the droplet can move even in a confined wettability track with $w^* = 0.1$.

The droplet footprint area increases with the increase in w^* as shown in the bottom view of Fig. 8. From the side view, it is observed that droplets become more elongated on increasing w^*. It is observed that for $w^* = 0.2$, droplet front takes $t^* = 23$ to reach the end of the track. On decreasing the wettability confinement by increasing the value of w^*, the droplet takes lesser time to reach the end of the track. Hence, the droplet is transported faster for
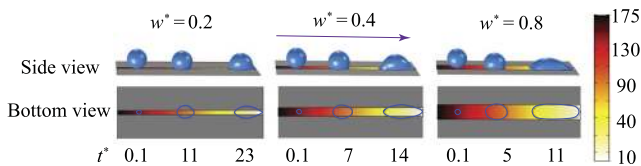

FIG. 8. A droplet is placed on a confined wettability gradient track having wettability confinement w^*. The droplet position and shape with different t^* are shown for three different w^*.

$w^* = 0.8$. Figure 9(a) shows that the final droplet footprint area is higher for $w^* = 0.8$ compared to other w^* values 0.2, 0.4, and 0.6. It should be noted that A^* is maximum for $w^* = 2$, as the confinement effect decreases with the increase in w^*. Figure 9(b) shows that the nondimensional height of the droplet h^* decreases with the nondimensional position of the droplet x^*. Height reduction is higher for $w^* = 0.8$ compared to other lower values of w^* because of less restriction on droplet spreading. The variation of A^* and h^* with t^* and x^*, respectively, are linear ($R^2 = 0.97$) because of linear variation of contact angle from upstream to downstream of the track as shown in Eq. (13). Figure 9(a) shows that nondimensional wetted area A^* increases with the increase in w^*. The inset of Fig. 9(a) shows the variation of slope of the curve m with w^*. It is observed that m decreases linearly from 0.303 to 0.19 on increasing the confinement from $w^* = 2$ to $w^* = 0.8$. Further confinement ($w^* \leq 0.8$) leads to a linear sharp reduction of m from 0.19 to 0.029. The rate of decrease in the slope m is less for $w^* = 2$ to $w^* = 0.8$ as compared to the rate of decrease in slope m for $w^* \leq 0.8$. This is because of the restriction on the spreading of the droplet for higher confinement (for smaller w^*). Figure 9(b) shows that nondimensional height h^* decreases with the increase in w^*. The inset of Fig. 9(b) represents the variation of m with w^*. It is observed that m increases linearly from −0.875 to −0.62 on increasing the confinement from $w^* = 2$ to $w^* = 0.8$. Further confinement ($w^* \leq 0.8$) leads to a sharp linear increase in the slope m from −0.62 to −0.212. The rate of increase in slope m is less for $w^* = 2$ to $w^* = 0.8$ as compared to the rate of increase in slope m for $w^* \leq 0.8$.

Figures 9(c) and 9(d) shows that there is a small increase in the average capillary number Ca_{avg} as we increase the confinement from $w^* = 2$ to $w^* = 0.8$. Further increase in wettability confinement w^* leads to a sharp reduction of droplet capillary number Ca. For a track of wettability gradient $\lambda = 23.5$, although it is possible to transport a droplet up to wettability confinement $w^* = 0.1$ but $w^* = 0.8$ is the most efficient wettability confinement. In the wettability gradient of the $\lambda = 23.5$ track, the average capillary number of the droplet Ca_{avg} is almost constant up to wettability confinement $w^* = 0.8$, and it decreases sharply with further increase in the wettability confinement as shown in Fig. 9(d).

D. Comparison of droplet transport characteristics on different wettability gradient tracks

In this work, droplet transport characteristics on different combinations of the wettability gradient track such as
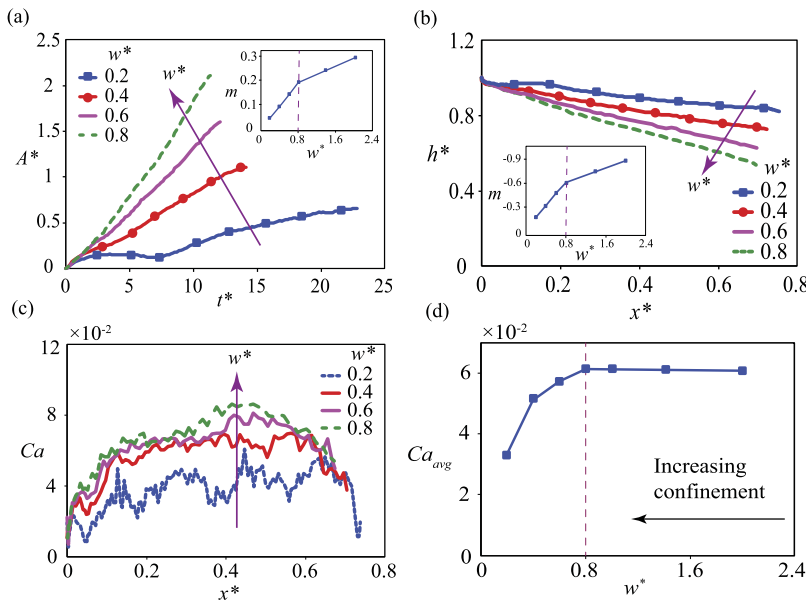
FIG. 9. (a) Nondimensional wetted area of the droplet A^* with nondimensional time t^* is plotted for different wettability confinements w^*. Slope of the linear part of each curve is represented by m. (b) The nondimensional height of the droplet h^* is plotted with the nondimensional position of the droplet x^* for different w^*. (c) Variation of capillary number of the droplet Ca with the nondimensional position x^* is plotted for different w^*. (d) Variation of average capillary number of the droplet Ca_{avg} with different w^* is plotted.

hydrophilic–superhydrophilic and hydrophobic/superhydrophobic-superhydrophilic are studied. All the cases are studied based on the wettability gradient (represented by λ) provided on the track. For example, wettability gradient λ = 11.5 and 23.5 represents hydrophilic–superhydrophilic and superhydrophobic–superhydrophilic wettability gradient, respectively. A wettability gradient λ in the range of 12–21.5 represents hydrophobic–superhydrophilic wettability gradient. Droplet behavior changes for different wettability gradients λ and wettability confinements (w^*) of the track. For λ ranging from 12 to 21.5, droplet velocity increases with the increase in λ. Droplet velocity almost becomes double for λ = 23.5 as compared to λ = 11.5. For λ = 11.5, confinement can be done up to $w^* \sim 0.3$, whereas for λ = 23.5, a confinement of $w^* \sim 0.1$ is possible. For a track with λ = 11.5, droplet spreading is higher compared to all other possible wettability gradients, and hence this group of wettability can be used for the application of droplet-based cooling techniques.

E. Regimes of droplet transport on wettability gradient confined track

We find that droplet behavior depends on the wettability gradient and confinement of the track. A regime plot of droplet transport is shown for different wettability gradients and confinements in Fig. 10. In the regime plot, wettability gradient λ ranges from 0 to 23.5. The droplet diameter is taken as d_0 = 0.5 mm. We identified three regimes based on the transport of the droplet, namely: (a) moving droplet, (b) stationary droplet, and (c) film. These three regimes are differentiated with the combination of wettability gradient and confinement values, as shown in Fig. 10. The regime in which droplets are transported without creating a film is called the moving droplet regime represented by (a) in Fig. 10. In this regime, droplets travel smoothly from the upstream to the downstream end of the track. It can be observed in Fig. 10 that the droplets do not

travel for wettability confinement w^* < 0.1 irrespective of the wettability gradient of the track. In this stationary droplet regime [regime (b)], the droplet footprint area is smaller because of the restriction on spreading due to the confinement. Thus, the driving force is not enough to transport the droplet. The droplets do not also get transported for wettability gradient λ < 4 with wettability confinement w^* < 0.6 because of the inadequate wettability gradient to drive the droplets. For $w^* \geq 0.6$ and λ approximately between 0 and 7.5, droplets become a thin film. The filming regime [regime (c)] is approximated when the droplet footprint length in the direction of droplet transport is greater than $3d_0$. As this criterion is imposed, the border of the film regime becomes sharp; this leads to a sharp transition from the moving droplet regime to the film regime and the stationary droplet regime to the film regime. However, there
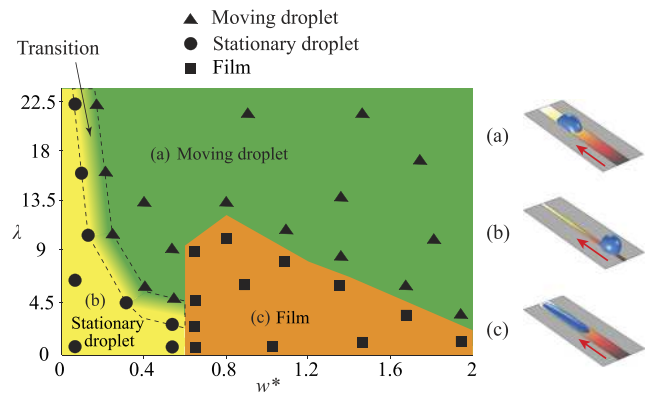

FIG. 10. Regimes of droplet transport are plotted for different wettability gradients λ and wettability confinements w^*. Downstream contact angle θ^L is fixed as 10°. The upstream contact angle θ^H varies from 175° to 10°. Length of the track is taken as L = 3.5 mm.

is a smooth transition from the stationary droplet to the moving droplet regime across the dashed line as shown in the regime plot in Fig. 10. The representative droplet images of each regime are shown in Fig. 10.

IV. CONCLUSION

Droplet transport on a confined wettability gradient surface is numerically investigated by considering negligible hysteresis on the surface. Droplet behavior changes for different wettability confinements and gradients of the track. In the hydrophilic wettability gradient track, the droplet moves in the track for the wettability confinement of $w^* > 0.3$. However, it is possible to transport the droplet for the wettability confinement up to $w^* \sim 0.1$ in the case of a superhydrophobic–superhydrophilic wettability gradient track. Droplet velocity was found to be the highest for the superhydrophobic–superhydrophilic wettability gradient track with a wettability confinement of $w^* = 0.8$. After studying the effect of wettability confinement and wettability gradient, it is observed that a droplet does not travel for wettability confinement $w^* < 0.1$ irrespective of the wettability gradient of the track. The droplet cannot also get transported for wettability gradient $\lambda < 4$ and wettability confinement $w^* < 0.6$. For wettability confinement, $w^* > 0.6$ and wettability gradient $\lambda < 7.5$, a droplet creates a thin film. The outcome of the present study provides the guidelines for the design of efficient droplet transport mechanisms by surface wettability control for lab-on-a-chip (LOC) systems and other microfluidic devices.

APPENDIX: FORCES INVOLVED DURING DROPLET TRANSPORT ON A WETTABILITY GRADIENT TRACK

In the present case, there are only two significant forces which govern the movement of the droplet. One is the driving force, F_d, due to the contact angle difference between the rear and front of the droplet. The other force is the hydrodynamic resistance force F_r which resists the droplet movement. The driving force F_d is[23]

$$F_d = 2\sigma R \int_0^{\frac{\pi}{2}} (\cos(\theta_e)_f - \cos(\theta_e)_b)\cos\phi\, d\phi \approx A\sigma \frac{d\cos\theta}{dx}. \quad (A1)$$

The resistive force F_r is[23]

$$F_r \approx \frac{6\pi R\mu_2 U}{\theta_{avg}}\ln(2\epsilon), \quad (A2)$$

where σ denotes the surface tension of the droplet, R is the wetted radius of the droplet, which is assumed as constant while deriving F_r by Subramanian et al.[23] The wetted area $A = \pi R^2$ is considered to be constant for deriving F_d by Subramanian et al.[23] The contact angle of the droplet with the wetted wall is $\theta_{avg} \approx ((\theta_e)_f + (\theta_e)_b)/2$. The front static contact angle of the droplet is $(\theta_e)_f$, and the rear static contact angle is $(\theta_e)_b$. The dimensionless parameter $\epsilon = l_{s1}/R$ represents the ratio of the slip length l_{s1} to the footprint radius or the wetted radius R of the droplet. The slip length is $l_{s1} = 0.5 \times 10^{-9}$.[23] The dynamic viscosity of the droplet is μ_2, and the velocity of the droplet is U. In the present case, the droplet stretching is significant and hence the wetted area is not circular so we modified Eqs. (A1) and (A2) by considering the transient wetted area of the droplet $A(t)$.

The approximated F_d and F_r are

$$F_d \approx A(t)\sigma \frac{d\cos\theta}{dx}, \quad (A3)$$

$$F_r \approx \frac{6\pi R(t)\mu_2 U}{\theta_{avg}(t)}\ln(2\epsilon). \quad (A4)$$

We have approximated $R(t) \sim \sqrt{A(t)}$, where $\theta_{avg}(t)$ is the average contact angle at which the droplet is exposed which is changing during the transport of the droplet, $\theta_{avg}(t) = ((\theta_e)_f(t) + (\theta_e)_b(t))/2$.

The resultant net force $(F_d - F_r)$ is responsible for the droplet transport which is equal to $m\frac{dU}{dt}$ as per Newton's law of motion

$$F_d - F_r = m\frac{dU}{dt}, \quad (A5)$$

where m is mass of the droplet. The driving force F_d can be scaled as

$$F_d \sim R(t)^2\sigma \frac{(\cos\theta^H - \cos\theta^L)}{L}. \quad (A6)$$

Similarly, F_r can be scaled as

$$F_r \sim \frac{\mu_2 UR(t)}{\theta_{avg}(t)}\ln\left(\frac{l_s}{R(t)}\right). \quad (A7)$$

The right-hand side of Eq. (A5) can be scaled as

$$m\frac{dU}{dt} \sim \rho R_0^3 \frac{U}{\tau}. \quad (A8)$$

R_0 is the initial droplet radius. The velocity of the droplet $U = x/\tau$, where x is the center position of the droplet. The reference time scale is considered to be τ. To obtain τ, we invoke the idea that at any instant, the transport is caused by the capillary or driving force F_d so that $m\frac{dU}{dt} \sim F_d \Rightarrow \frac{mx}{\tau^2} \sim R(t)^2\sigma \frac{(\cos\theta^H - \cos\theta^L)}{L}$ $\Rightarrow \tau \sim L\sqrt{\frac{\rho R(t)x^*}{\sigma(\cos\theta^H - \cos\theta^L)}}$. Here, $x^* = \frac{x}{L}$. The velocity of the droplet U can be replaced by the capillary number of the droplet Ca by using the expression $Ca = \mu_2 U/\sigma$. By using the scaled expression of F_d, F_r, and $m\frac{dU}{dt}$ and also the expression of Ca in Eq. (A5), we will get the following scaled expression of Ca:

$$Ca \sim \frac{\left(\frac{R(t)^2}{L}\right)(\cos\theta^H - \cos\theta^L)}{\frac{\rho R_0^3}{\mu_2\tau} + \frac{R(t)\ln(l_s/R(t))}{\theta_{avg}(t)}}, \quad (A9)$$

$$Ca = K_1\frac{\left(\frac{R(t)^2}{L}\right)(\cos\theta^H - \cos\theta^L)}{\frac{\rho R_0^3}{\mu_2\tau} + \frac{R(t)\ln(l_s/R(t))}{\theta_{avg}(t)}}, \quad (A10)$$

where K_1 is a fitting parameter whose value is 2.32 (with $R^2 \sim 0.9$). Equation (A10) gives the variation of Ca for different wettability gradients $\sim (\cos\theta^H - \cos\theta^L)d_0/L$ with different wetted radii $R(t)$. Figure 11 shows the variation of both scaled Ca [using Eq. (A10)] and numerical Ca (using simulation results) during the transport of the droplet for two different wettability gradients 11.5 and 23.5 having $w^* = 2$. For wettability gradient 11.5, scaled and numerical Ca follow the same trend as shown in Fig. 11(a). The small jump in the
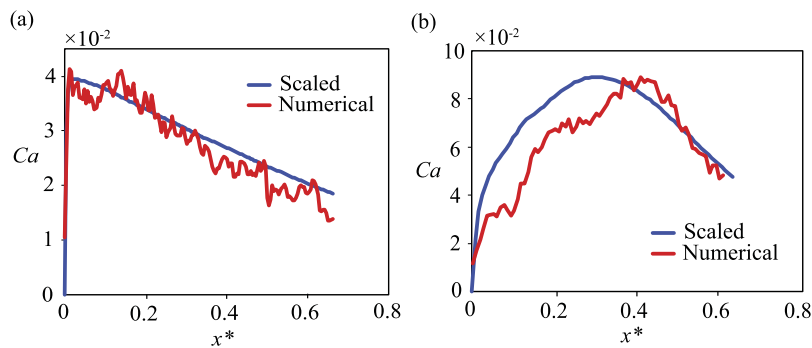
FIG. 11. (a) Variation of the scaled Ca and the numerical Ca of the droplet is plotted with the nondimensional position of the droplet x^* for wettability gradient λ = 11.5 and wettability confinement w^* = 2. (b) Variation of the scaled Ca and the numerical Ca of the droplet is plotted with x^* for λ = 23.5 and w^* = 2.
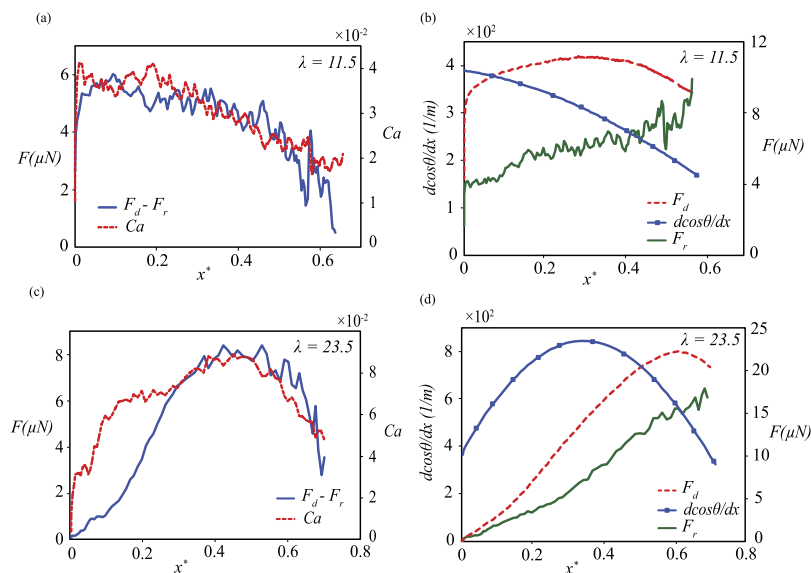

FIG. 12. (a) Variation of the net driving force ($F_d - F_r$) and capillary number of the droplet Ca is plotted with the nondimensional position of the droplet x^* for λ = 11.5 and w^* = 2. (b) Variation of F_d, F_r, and $d \cos \theta / dx$ with x^* is plotted for λ = 11.5 and w^* = 2. (c) Variation of the net driving force ($F_d - F_r$) and Ca is plotted with x^* for λ = 23.5 and w^* = 2. (d) Variation of F_d, F_r, and $d \cos \theta / dx$ with x^* is plotted for λ = 23.5 and w^* = 2.

numerical Ca in the initial part of the curve is due to the initial sharp spreading of the droplet, which is not accounted in the scaling of Ca. For wettability gradient 23.5, the Ca increases up to x^* = 0.4 and decreases further as shown in Fig. 12(b).

As shown in Figs. 12(a) and 12(c), the magnitude of ($F_d - F_r$) increases initially, and after some distance, it decreases. The droplet velocity reaches its maximum velocity when the magnitude of ($F_d - F_r$) is maximum. This is true for both λ = 11.5 and 23.5. The variation of ($F_d - F_r$) and Ca with x^* also follows a similar trend as shown in Figs. 12(a) and 12(c). The variation of F_d, F_r, and $d \cos \theta/dx$ with x^* is shown in Figs. 12(b) and 12(d) for λ = 11.5 and 23.5, respectively. The driving force F_d is dependent on $A(t)$ and $d \cos \theta/dx$ as shown in Eq. (A3). $A(t)$ increases continuously during the transport of the droplet. Initially, the decrease in $d \cos \theta/dx$ is slow compared to the increase in $A(t)$. This results in the increase in F_d up to x^* = 0.3 as shown in Fig. 12(b). After that, because of the sharp reduction of $d \cos \theta/dx$ and slow increase in $A(t)$, F_d decreases for $x^* \geqslant 0.3$.

As shown in Eq. (A4), the resistive force F_r is dependent on the velocity of the droplet U and the wetted radius $R(t) \sim \sqrt{A(t)}$. The continuous increase in $R(t)$ along the direction of droplet transport makes F_r to increase continuously. F_r will also increase on increasing

U, however, the effect of $R(t)$ is more significant than U. Therefore, the combined effect of U and $R(t)$ makes the F_r to increase.

REFERENCES

[1] X. Yao, Y. Song, and L. Jiang, "Applications of bio-inspired special wettable surfaces," Adv. Mater. **23**(6), 719–734 (2011).

[2] J. Li and Z. Guo, "Spontaneous directional transportations of water droplets on surfaces driven by gradient structures," Nanoscale **10**(29), 13814–13831 (2018).

[3] A. Ghosh, R. Ganguly, T. M. Schutzius, and C. M. Megaridis, "Wettability patterning for high-rate, pumpless fluid transport on open, non-planar microfluidic platforms," Lab Chip **14**(9), 1538–1550 (2014).

[4] A. A. Darhuber, J. P. Valentino, S. M. Troian, and S. Wagner, "Thermocapillary actuation of droplets on chemically patterned surfaces by programmable microheater arrays," J. Microelectromech. Syst. **12**(6), 873–879 (2003).

[5] S. Mettu and M. K. Chaudhury, "Motion of drops on a surface induced by thermal gradient and vibration," Langmuir **24**(19), 10833–10837 (2008).

[6] M. Foroutan, S. M. Fatemi, F. Esmaeilian, V. Fadaei Naeini, and M. Baniassadi, "Contact angle hysteresis and motion behaviors of a water nanodroplet on suspended graphene under temperature gradient," Phys. Fluids **30**(5), 052101 (2018).

[7] V. Jaiswal, A. Harikrishnan, G. Khurana, and P. Dhar, "Ionic solubility and solutal advection governed augmented evaporation kinetics of salt solution pendant droplets," Phys. Fluids **30**(1), 012113 (2018).

[8] S. K. Cho, H. Moon, and C.-J. Kim, "Creating, transporting, cutting, and merging liquid droplets by electrowetting-based actuation for digital microfluidic circuits," J. Microelectromech. Syst. **12**(1), 70–80 (2003).

[9] L. Latorre, J. Kim, J. Lee, P.-P. De Guzman, H. J. Lee, P. Nouet, and C.-J. Kim, "Electrostatic actuation of microscale liquid-metal droplets," J. Microelectromech. Syst. **11**(4), 302–308 (2002).

[10] G. Kunti, P. K. Mondal, A. Bhattacharya, and S. Chakraborty, "Electrothermally modulated contact line dynamics of a binary fluid in a patterned fluidic environment," Phys. Fluids **30**(9), 092005 (2018).

[11] G. Kunti, A. Bhattacharya, and S. Chakraborty, "Electrothermally actuated moving contact line dynamics over chemically patterned surfaces with resistive heaters," Phys. Fluids **30**(6), 062004 (2018).

[12] Z. Long, A. M. Shetty, M. J. Solomon, and R. G. Larson, "Fundamentals of magnet-actuated droplet manipulation on an open hydrophobic surface," Lab Chip **9**(11), 1567–1575 (2009).

[13] K. Ichimura, S.-K. Oh, and M. Nakagawa, "Light-driven motion of liquids on a photoresponsive surface," Science **288**(5471), 1624–1626 (2000).

[14] Y. Zheng, J. Cheng, C. Zhou, H. Xing, X. Wen, P. Pi, and S. Xu, "Droplet motion on a shape gradient surface," Langmuir **33**(17), 4172–4177 (2017).

[15] J. M. Morrissette, P. S. Mahapatra, A. Ghosh, R. Ganguly, and C. M. Megaridis, "Rapid, self-driven liquid mixing on open-surface microfluidic platforms," Sci. Rep. **7**(1), 1800 (2017).

[16] S. Dhiman, K. Jayaprakash, R. Iqbal, and A. K. Sen, "Self-transport and manipulation of aqueous droplets on oil-submerged diverging groove," Langmuir **34**(41), 12359–12368 (2018).

[17] R. J. Petrie, T. Bailey, C. B. Gorman, and J. Genzer, "Fast directed motion of fakir droplets," Langmuir **20**(23), 9893–9896 (2004).

[18] X. Xu and T. Qian, "Droplet motion in one-component fluids on solid substrates with wettability gradients," Phys. Rev. E **85**(5), 051601 (2012).

[19] O. Hegde, S. Chakraborty, P. Kabi, and S. Basu, "Vapor mediated control of microscale flow in sessile droplets," Phys. Fluids **30**(12), 122103 (2018).

[20] J.-T. Yang, J. C. Chen, K.-J. Huang, and J. A. Yeh, "Droplet manipulation on a hydrophobic textured surface with roughened patterns," J. Microelectromech. Syst. **15**(3), 697–707 (2006).

[21] H. P. Greenspan, "On the motion of a small viscous droplet that wets a surface," J. Fluid Mech. **84**(1), 125–143 (1978).

[22] F. Brochard, "Motions of droplets on solid surfaces induced by chemical or thermal gradients," Langmuir **5**(2), 432–438 (1989).

[23] R. S. Subramanian, N. Moumen, and J. B. McLaughlin, "Motion of a drop on a solid surface due to a wettability gradient," Langmuir **21**(25), 11844–11849 (2005).

[24] M. K. Chaudhury and G. M. Whitesides, "How to make water run uphill," Science **256**(5063), 1539–1541 (1992).

[25] N. Moumen, R. S. Subramanian, and J. B. McLaughlin, "Experiments on the motion of drops on a horizontal solid surface due to a wettability gradient," Langmuir **22**(6), 2682–2690 (2006).

[26] M. K. Chaudhury, A. Chakrabarti, and S. Daniel, "Generation of motion of drops with interfacial contact," Langmuir **31**(34), 9266–9281 (2015).

[27] O. Bliznyuk, H. P. Jansen, E. S. Kooij, H. J. Zandvliet, and B. Poelsema, "Smart design of stripe-patterned gradient surfaces to control droplet motion," Langmuir **27**(17), 11238–11245 (2011).

[28] Y. Ito, M. Heydari, A. Hashimoto, T. Konno, A. Hirasawa, S. Hori, K. Kurita, and A. Nakajima, "The movement of a water droplet on a gradient surface prepared by photodegradation," Langmuir **23**(4), 1845–1850 (2007).

[29] C. Liu, J. Sun, J. Li, C. Xiang, L. Che, Z. Wang, and X. Zhou, "Long-range spontaneous droplet self-propulsion on wettability gradient surfaces," Sci. Rep. **7**(1), 7552 (2017).

[30] Q. Liu and B. Xu, "A unified mechanics model of wettability gradient-driven motion of water droplet on solid surfaces," Extreme Mech. Lett. **9**, 304–309 (2016).

[31] K. A. Raman, "Dynamics of simultaneously impinging drops on a dry surface: Role of inhomogeneous wettability and impact shape," J. Colloid Interface Sci. **516**, 232–247 (2018).

[32] J.-J. Huang, H. Huang, and X. Wang, "Numerical study of drop motion on a surface with stepwise wettability gradient and contact angle hysteresis," Phys. Fluids **26**(6), 062101 (2014).

[33] M. Ahmadlouydarab and J. J. Feng, "Motion and coalescence of sessile drops driven by substrate wetting gradient and external flow," J. Fluid Mech. **746**, 214–235 (2014).

[34] J. Huang, C. Shu, and Y. Chew, "Numerical investigation of transporting droplets by spatiotemporally controlling substrate wettability," J. Colloid Interface Sci. **328**(1), 124–133 (2008).

[35] M. Sussman, P. Smereka, and S. Osher, "A level set approach for computing solutions to incompressible two-phase flow," J. Comput. Phys. **114**(1), 146–159 (1994).

[36] Y. Dai, Z. Zhou, J. Lin, and J. Han, "Modeling of two-phase flow in rough-walled fracture using level set method," Geofluids **2017**, 2429796.

[37] H. Grzybowski and R. Mosdorf, "Modelling of two-phase flow in a minichannel using level-set method," J. Phys.: Conf. Ser. **530**, 012049 (2014).

[38] C. Multiphysics, Comsol multiphysics CFD module user guide (version 5.3 a), COMSOL, 2015, 208–265.

[39] H. Matsui, Y. Noda, and T. Hasegawa, "Hybrid energy-minimization simulation of equilibrium droplet shapes on hydrophilic/hydrophobic patterned surfaces," Langmuir **28**(44), 15450–15453 (2012).